communications materials

ARTICLE

https://doi.org/10.1038/s43246-022-00271-1 OPEN

Probing the evolution of electronic phase-coexistence in complex systems by terahertz radiation

Gulloo Lal Prajapati[1,2], Sarmistha Das[1,2], Rahul Dagar[1], V. Eswara Phanindra[1] & Dhanvir Singh Rana[1✉]

In complex oxides, electrons under the influence of competing energetics determine the coexistence or phase-separation of two or more electronic or magnetic phases within the same structural configuration. Probing the growth and evolution of such phase-coexistence state is crucial to determine the correct mechanism of related phase transition. Here, we demonstrate the combination of terahertz (THz) time-domain spectroscopy and DC transport as a strategy to probe the electronic phase-coexistence. This is demonstrated in disorder-controlled phase-separated rare-earth nickelate thin films, which exhibit a temperature induced metal-insulator transition in DC conductivity but lack this transition in THz dynamic conductivity. Such pronounced disparity exploits two extreme attributes, namely, the large sensitivity of THz radiation to a spatial range of the order of its wavelength-compatible electronic inhomogeneities, and its insensitivity to a range beyond the size of its wavelength. This feature is generic in nature, depending solely on the size of insulating and metallic clusters. Therefore, our strategy offers a high-sensitivity methodology to investigate electronic phase-coexistence and phase transition in a wide range of complex material systems.

[1] Department of Physics, Indian Institute of Science Education and Research (IISER), Bhopal, Madhya Pradesh 462066, India. [2] These authors contributed equally: Gulloo Lal Prajapati, Sarmistha Das. ✉email: dsrana@iiserb.ac.in

The spatial coexistence of multiple phases in a degenerate state is one of the basic features of transition metal oxides (TMOs)[1–3]. Usually in TMOs, different lattice, charge, spin, and orbital degrees of freedom are inter-coupled which hinders the onset of the sharp phase transition. Consequently, for a range of perturbation values around the transition point, phase-coexistence of multiple phases occurs at the nano to micrometer length scale. In the phase-coexistence region, all the phases are fragile. Thus, even a slight change in external perturbation can cause substantial changes in their strengths and spatial distributions. Hence, probing the growth and evolution of the phase-coexistence state with a variation of the external perturbation plays a crucial role in determining the exact mechanism of phase transitions. Some recent examples are as follows: (i) by imaging the growth of the metal-insulator coexistence phase in VO_2, Qazilbash et al.[4] revealed that the response of metallic puddles in the phase-coexistence region is different from the pure metallic phase and concluded that the metal-insulator transition (MIT) in VO_2 is accompanied by the mass divergence of charge carriers in the vicinity of transition temperature (T_{MI}). (ii) Post et al.[5] showed a continuous domain wall formation (a second-order phase transition) along with an abrupt transition of insulating domains to metallic domains (a first-order phase transition) at the onset of MIT during warming in rare earth nickelates ($RNiO_3$). This is a rare example of the coexistence of first- and second-order phase transitions in the whole class of TMOs. (iii) Phase-coexistence in manganites suggests that the magnetoresistance behavior should be viewed as percolation of metallic ferromagnetic domains into an insulating phase[6]. (iv) Experiments reveal that a partial gap in the density of state exists for a range of temperatures above T_C which provides the microscopic basis for the understanding of fluctuating superconducting response above T_C in hole-doped high-T_C superconductors[7]. Such important breakthroughs from time to time have continuously kept surprising as one goes deeper to understand the complexity in TMOs associated with the co-existence of multiple phases.

Probing of the evolution of phase-coexistence and unveiling the underlying physics requires the development of novel experimental techniques and strategies. Indirect probes such as DC electrical transport and magnetometry show a substantial effect on the evolution of phase-coexistence on the measured data, however, they fail to extract microscopic details of the onset of phase-coexistence[8,9]. On the other hand, direct spatial probes such as scanning tunneling microscope and spectroscopy, transmission electron microscopy, scanning near field infrared microscopy, etc., provide real-space visualization of phase transitions and formation of phase-coexistence states, thus provide better understanding of phase transition[4–7,10–13]. Though, the probing of the phase-coexistence state may be limited by several factors such as sample preparation in desired state and conditions, the need for equipment that might be very costly and geographically unfavorable or need of specialized expertise. Therefore, it is always in demand to develop new experimental tools and methodology which are simple, cost effective, widely available, and last but not the least, can provide results in lesser time with high precision. Here, we present a combination of THz time-domain spectroscopy (THz-TDS) and DC transport as a methodology which can indirectly probe the intricate electronic phase-separation and its modulation with external perturbations.

We fabricated a number of nickelate thin films consisting of different insulating/metallic cluster sizes in the phase-coexistence region by incorporating different types and amount of disorder into the films. Our results are twofold: the DC transport measurement detects the onset of temperature-induced MIT in all the films regardless of type and amount of disorder present in the films while the THz transport detects gradual weakening of MIT as the disorder in the film increases. After a critical strength of disorder, the MIT in THz transport measurement completely disappears and shows only metallic signature down to the lowest temperature. This result in itself is very surprising at first glance as one expects a similar electronic state, at least, qualitatively for the films when probed by DC and THz transport techniques. We subsequently verified that the detection of such metallic state in THz transport is not the mere outcome of photo-induced effect and the deviation in the two electronic transports occurs (qualitatively) only in the films exhibiting electronic phase-coexistence below T_{MI}. Thereafter, we established that this feature solely depends on the insulating/metallic cluster sizes in the phase-coexistence state; no matter how one achieves the phase-coexistence. Thus, this feature is generic in nature and true for electronic phase-coexistence in any material system. The methodology introduced here, therefore, can serve as a tool to investigate electronic phase-coexistence present in any system and reveal the possible underlying mechanism related to the complex phase transitions.

Results and discussion

Different electronic states below T_{MI}, probed by DC and THz transports. In the present study, we prepared three sets of films: (i) three films with varying strengths of disorder exhibiting MIT of different strengths (set 1): $PrNiO_3$ (PNO) on $NdGaO_3$ (NGO) (100) [PNO/NGO], $La_{0.5}Eu_{0.5}NiO_3$ (LENO) on NGO (100) [LENO/NGO] and on (LSAT) (100) [LENO/LSAT]; (ii) two films without any MIT down to low temperature (set 2): LENO on $LaAlO_3$ (LAO) (100) [LENO/LAO] and $LaNiO_3$ (LNO) on LAO (100) [LNO/LAO] and (iii) three films having a moderate amount of cation disorder, one of them, in addition, has the mosaic disorder, all exhibiting MIT (set 3): $Pr_{0.5}Sm_{0.5}NiO_3$ (PSNO) on LAO (100) [PSNO/LAO] with thicknesses of 40 nm and 80 nm and PSNO on mosaic LAO (100) with a thickness of 40 nm [see the Table 1]. A comparison of resistivities (ρ) as a function of

Table 1 Description of $RNiO_3$ films used in DC transport and THz-TDS measurements.

	Thin films	Thickness (~nm)	Types of disorder	T_{MI}
Set 1	PNO/NGO (100)	30	Oxygen vacancies	130 K
	LENO/NGO (100)	30	Oxygen vacancies + cation disorder	180 K
	LENO/LSAT (100)	30	Oxygen vacancies + cation disorder	150 K
Set 2	LNO/LAO (100)	30	Oxygen vacancies	No MIT
	LENO/LAO (100)	30	Oxygen vacancies + cation disorder	No MIT
Set 3	PSNO/LAO (100)_40 nm	40	Oxygen vacancies + cation disorder	209 K
	PSNO/LAO (100)_80 nm	80	Oxygen vacancies + cation disorder	190 K
	PSNO/LAO (100)_mosaic	40	Oxygen vacancies + cation disorder + mosaic disorder	150 K

T_{MI} were determined via DC transport.

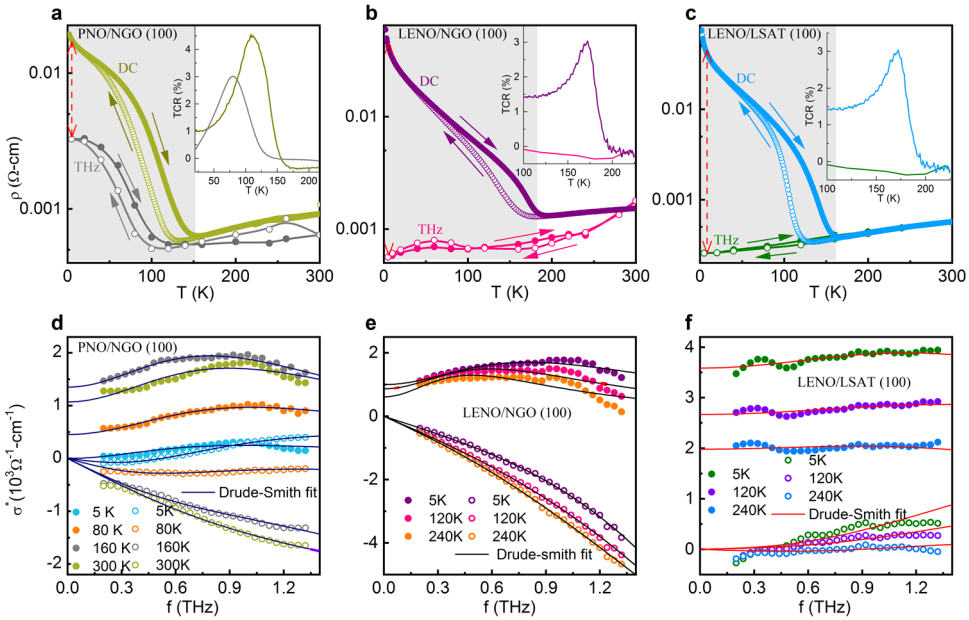

Fig. 1 Comparative representation of dc and THz resistivities as a function of temperature and THz frequency-dependent carrier dynamics. **a**–**c** Comparison of resistivities obtained from DC and THz transport (at 1 THz). The shaded region indicates the prominent difference between DC and THz resistivities below the T_{MI}. Insets show temperature coefficient of resistivity (TCR; $\mathrm{TCR}(\%) = \frac{-1}{\rho}\frac{d\rho}{dT} \times 100$) plots in heating protocol. The temperature corresponding to maximum of TCR(%) is the T_{MI} of the film. **d**-**f** Complex conductivity (σ^*) vs THz frequency spectra: the filled and void symbols represent the real (σ_1) and imaginary (σ_2) components of σ^*, respectively. The solid lines are the fitted curves using Drude-Smith model.

temperature (T) for different films of set 1, measured in DC and THz (at 1 THz) transports, are shown in Fig. 1a–c. THz dynamic resistivity ($\rho(f)$) was determined using the relation $1/\sigma_1(f) = \rho(f)$; where $\sigma_1(f)$ is the real part of complex THz conductivity ($\sigma^*(f)$) at frequency 'f'. Clearly, for PNO/NGO film, both DC and THz resistivities exhibit MIT at ~130 K (Fig. 1a). Here, above T_{MI} in the metallic region, the DC and THz resistivities are nearly the same, while below T_{MI}, at the onset of phase-coexistence state, the THz resistivity starts differing from the DC resistivity. The THz resistivity is about one order of magnitude lower than its DC counterpart at the lowest measured temperature. This feature becomes more pronounced in the LENO/NGO and LENO/LSAT films (Fig. 1b, c). It is clearly seen that both these films exhibit MIT in the DC transport while the MIT in THz transport gradually weakens; for the LENO/LSAT film, only metallic behavior is observed in the entire temperature range. This is the first observation of such a stark difference between the electronic states probed by DC and THz transports. In general, one expects to observe similar temperature-dependent electronic (insulating/metallic) states when the film is probed by DC and THz transports. The THz-TDS being non-contact technique, may give slightly lower resistivity compare to DC measurement, however, the qualitative behavior of the film (i.e. insulating/metallic nature) is still expected to be the same in both the transport techniques. Especially when the given energy of used THz radiation (~0.8–6 meV) is much lower compared to the known charge-transfer gap of nickelates (~1–2 eV). Hence, the probing of different electronic states below the T_{MI} in DC and THz transports (insulating and metallic states, respectively) can raise several curiosities, such as: how is probing of different electronic states by the two techniques related to disorders present in the films? Is it related to disorder modulated phase-coexistence state or is photo-induced effect in THz transport which possibly generates sufficient charge carriers thus, converting the insulating state into a metallic state? We discuss such a prospective in detail as described below.

Role of disorder. The thermal hysteresis of first-order MIT is always susceptible to various types of disorder. In nickelates, such hysteresis as well as the electronic states above and below the MIT are very sensitive to the oxygen vacancies and the quenched disorder[14,15]. In the films PNO/NGO, LENO/NGO and LENO/LSAT, a combination of these two factors is responsible for introducing different levels of disorder. While PNO/NGO film is oxygen deficient, the disorders in LENO/NGO and LENO/LSAT are introduced by a combination of both, quenched disorder and oxygen deficiency. In LENO/NGO and LENO/LSAT, the quenched disorder manifests due to the large cation size mismatch of La^{3+} (1.216 Å) and Eu^{3+} (1.120 Å)[15]. As larger tensile strain tends to develop larger oxygen vacancies in perovskite oxides, LENO/LSAT [deposited on LSAT (100)] will be the more disordered film compared to LENO/NGO [deposited on NGO (001)][16–18]. Hence, expected disorder strength in ascending order is from PNO/NGO to LENO/LSAT.

We further determined the strength of disorder quantitatively by analyzing complex THz conductivity spectra of the films. The complex THz conductivity (σ^*) vs THz frequency (f) spectra at different temperatures for the films of set-1 are plotted in Fig. 1d–f. It is clear from the spectra that the real component ($\sigma_1(f)$) of σ^* for all the films deviate from the standard Drude model as the zero-frequency peaks are shifted to the higher frequency region. Also, the imaginary component ($\sigma_2(f)$) is dropped down to negative values at all temperatures, defying the conventional Drude-like free charge carrier behavior. Thus, the Drude-Smith (D-S) model was employed to explain such THz conductivity. As per D-S model, the σ^* follows the relation: $\sigma^* = \frac{\epsilon_0\omega_p^2\tau}{1-i\omega\tau}\left[1+\frac{c}{1-i\omega\tau}\right] - i\epsilon_0\omega(\epsilon_\infty - 1)$[19–21]. Here, ϵ_0 is permittivity of vacuum, ϵ_∞ is the permittivity of the medium at higher frequency, ω_p is plasma frequency, τ is scattering time of the charge carriers and c is the persistence of velocity parameter which accounts the strength of disorder present in the system. The value of c ranges from '0' to '−1'. For $c = 0$, D-S model reduces to the Drude model while non-zero negative value of c

signifies the presence of disorder in the system. The larger is the (negative) value of '*c*', stronger is the disorder. As shown in Fig. 1d–f, both σ_1 and σ_2 were simultaneously well-fitted to the D-S model. At 5 K, the disorder parameter '*c*' was determined as −0.47, −0.69 and −0.71 for PNO/NGO, LENO/NGO, and LENO/LSAT films, respectively. Hence, it is clear from the analysis that all the films possess disorder and the strength of disorder does follow the same trend as we inferred qualitatively in the previous section. Increasing disorder naturally increases electronic inhomogeneity in the system which subsequently leads to the strengthening of the phase-coexistence state. This suggests that the weakening of MIT in THz transport increases upon increasing the strength of the phase-coexistence state which finally results in a completely metallic state for the LENO/LSAT film.

Phase-coexistence as the origin of probing different electronic states. To further confirm the phase-coexistence as the origin of the occurrence of different electronic states below T_{MI} when probed by the DC and THz transports, it requires to compare DC and THz resistivities of nickelate films sans phase-coexistence. In this context, two compressive strained films, i.e., LNO and LENO, deposited on LAO (100) substrate [set 2], both are metallic down to 5 K (in DC transport), were investigated. Thus, these films are free from phase-coexistence and have only dominating single electronic state. Temperature dependences of DC and THz resistivities of these films are plotted in Fig. 2a. It is evident that both the films not only exhibit the single electronic state, i.e., metallic state down to low temperature but also the DC and THz resistivities are nearly superimposing on each other. Detection of the same electronic state in both the probing techniques confirms that the earlier observed disparity between the electronic states below the T_{MI} probed by DC and THz transports in the PNO/NGO, LENO/NGO, and LENO/LSAT films, is related to the disorder modulated phase-coexistence state.

However, it is imperative to consider the effect of photo-induced excitations on these films in THz transport measurements, because, the insulating state of nickelates is very likely to be associated with the formation of the charge-density-wave (CDW)[22–26]. In general, such CDW energy gap lies in the range of 1–5 meV. Hence, the THz photons are very well capable of closing this gap by breaking the charge-ordered insulating state. In such case, a metallic state can set in with a vivid resonance behavior in the $\sigma_1(f)$ spectra[22–26]. However, no CDW-like resonance absorption peak was observed in THz conductivity-frequency spectra (Fig. 1d–f). In this context, it is also worth mentioning that one can expect another possibility concerning the closing of the charge transfer gap between O-*2p* and Ni-*3d* upper Hubbard bands due to the THz photo-excitation. However, this is not possible in the present scenario as for nickelates, the charge-transfer gap lies in the energy range of ~1-2 eV[27] while the used energy range of THz band in our case is ~0.8-6 meV, i.e., nearly three orders of magnitude lower than the charge transfer gap energy. Further, the strength of the THz pulse used, is also very weak (E_{THz} ~ a few V/cm). Thus, such THz photons by themselves are not capable to cause photo-induced charge carrier generation. Nevertheless, to discard this possibility, we performed THz measurements on the LENO/LSAT film at 10 K (in insulating state) with three different DC bias voltage applied to THz emitter thus, emitting THz pulses with different pulse intensity. As shown in Fig. 2b, both the σ_1 and σ_2 spectra nearly overlap for all the three cases and do not exhibit any resonance peak-like signature. These results completely rule out any assumed possible photo-induced effect for the detection of metallic state in THz transport[28].

Interplay between phase-coexistence and probing wavelengths of THz band. Now, we attempt to draw a clear picture of the role of phase-coexistence and the inherent attributes of the optical THz-TDS technique in probing the metallic state below T_{MI}. To explain this feature, we invoke the attributes of the spatial distribution of THz wavelengths used in the measurements and evolution of insulating/metallic cluster sizes during the phase transition. To visualize this effect, a schematic is presented in Fig. 2c. The DC transport measurement is usually acquired in the four-probe contact method where itinerant charge carriers (electrons/holes) move towards respective electrodes upon applying a voltage difference across the two electrodes (Fig. 2d).

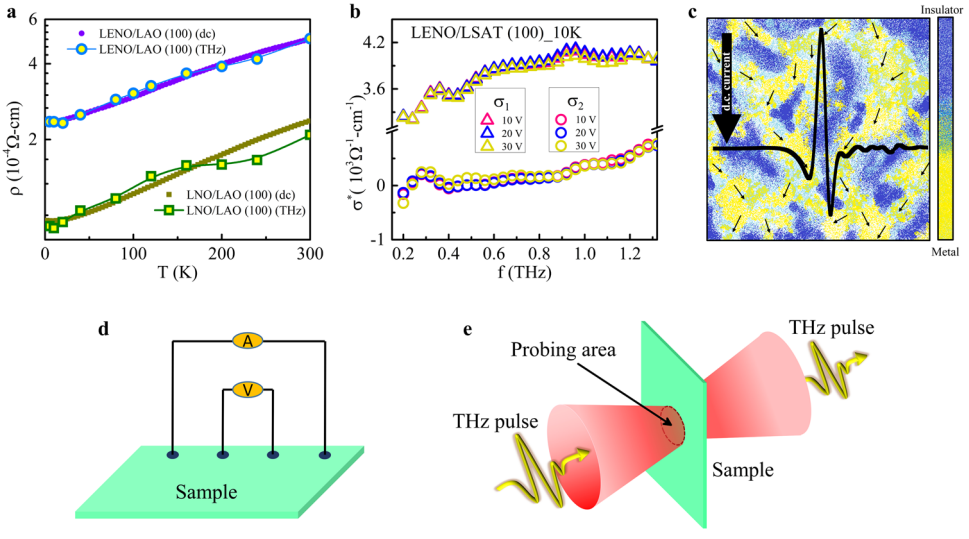

Fig. 2 Comparative representation of dc and THz resistivities, power-dependence of THz conductivity, and explanation of transport methodologies. **a** Comparison of resistivities obtained from DC and THz transport (at 1 THz) as a function of temperature for LNO/LAO (100) and LENO/LAO (100) films. **b** σ^* vs f spectra with THz emitter bias voltage variation for LENO/LAST (100) film at 10 K. **c** The schematic representation of phase-separated state consisting of insulating and metallic clusters. The small black arrows depict how the charge carriers get scattered in insulating clusters or trapped in defects in DC transport, whereas the THz waveform gives a nearly similar average transmission in the local limit. **d**, **e** Schematic representation of DC and THz transport methodology, respectively.

In this case, DC transport acts as a global probe since carriers from the entire volume of the sample participate in the electronic conduction. During their motion, these charge carriers get affected by all the insulating/metallic domains (irrespective of domain sizes) distributed over the entire volume via the scattering process. Thus, their response depends only on the volume fraction of insulating/metallic clusters. When the volume fraction of insulating clusters, upon cooling the nickelate film, exceeds to that of metallic clusters, the DC transport detects MIT in the film.

In contrast, THz transport is a non-contact measurement where data is acquired by the optical attributes, such as the wavelength of the THz radiation. In a THz-TDS experiment, the response of the THz pulse to a sample is determined by the microscopic currents occurring on nm length scales. As the charge carriers accelerated by the THz pulse cannot move far (usually they move up to 10's of nanometer only), the THz transport works as a local probe (Fig. 2e). Within the probing area, if the size of a cluster is compatible or greater than the probing wavelengths of THz pulse (200–1500 μm in the current case) then the transmitted THz pulse will be greatly affected by that cluster and will give an expected response. On the other hand, if the size of the cluster is smaller than the probing wavelengths of the THz pulse then THz pulse will overlook that cluster and will give an average response (at a given temperature and THz frequency). Thus, the response of the THz pulse to the phase-separation depends not only on insulating/metallic volume fractions but on their cluster size distributions as well. Now, starting from room temperature (i.e., from the metallic state), upon cooling the nickelate films, metallic domains transition into insulating domains. For least disordered PNO/NGO film, the MIT is sharp and smooth, so a large number of insulating clusters will grow upon cooling below the T_{MI} whose sizes are compatible or greater than the probing wavelengths. Hence, THz transport detects the MIT in the least disorder film. Introducing a disorder, in general, hinders the onset and growth of any phase and increases electronic inhomogeneity in the system. Therefore, the number of such insulating clusters whose sizes are compatible or greater than the THz probing wavelengths, decreases upon increasing disorder in the film. Consequently, the sharpness of the MIT successively decreases in THz transport (e.g., in LENO/NGO film). Above a critical strength of disorder, the number of such insulating clusters upon cooling is significantly low, hence the response of metallic clusters dominates. Thus, THz transport detects only metallic states above a critical strength of disorder (e.g., in LENO/LSAT film). It is worth mentioning here that Lai et al.[29], in a similar context, suggested the superiority of AC current imaging in local limit with respect to the DC measurement for analyzing the local resistivity of the materials having phase-coexistence state. In this framework, the THz spectroscopy is proven to be even advanced non-contact tool to probe ac conductivity in local limit.

We further note that the THz and DC resistivities match with each other for the LNO/LAO and LENO/LAO films which do not possess any phase-coexistence state and exhibit metallic state down to low temperatures. Combining all these observations together, this study reveals the extraordinary sensitivity of the THz technique to the phase-coexistence; making it an indispensable technique for multi-faceted studies of complex systems in which various competing interactions define the evolution of exotic properties. At this stage, it is important to investigate the generic nature of this feature whether it can be realized in other nickelate systems or not.

Generic nature of the response of phase-coexistence to THz-TDS. We investigated transport properties of moderately disordered PSNO/LAO films (40 and 80 nm), having relatively smaller cation size mismatch ($Pr_{0.5}Sm_{0.5}NiO_3$: $r_{Pr^{3+}} = 1.179$ and $r_{Sm^{3+}} = 1.132$) compared to $La_{0.5}Eu_{0.5}NiO_3$ films. The THz resistivities of these films at 1 THz, for both in cooling and heating protocols are plotted along with the corresponding DC resistivities in Fig. 3a, b. In heating protocol, the THz resistivity exhibits a subtle MIT and the magnitude of the THz resistivity is less than the DC resistivity at all temperatures. In contrast, the THz resistivity in cooling protocol is very different. With lowering the temperature, first MIT sets in ~120 K but again the metallic phase reappears upon further cooling (shaded region in Fig. 3). This behavior is well-consistent at all the THz frequencies as shown in Fig. 3c, d. The sudden fall of the THz resistivity curves in cooling protocol at around 100 K suggests the re-ordering/re-crystallization of the charge-ordered insulating state and occurrence of kinetically arrested phase transition[30–32]. This implies a spatial re-distribution of insulating and metallic clusters as well as a substantial increase in the size of metallic clusters in a phase-coexistence state below 100 K. Importantly, this feature is not detected by the DC transport and the reason again lies in the compatibility of the THz probing wavelengths with the size of insulating/metallic clusters. At the onset of MIT, the insulating phase first grows and then weakens at the cost of the growth of the metallic phase; thus, suggesting the re-distribution in the size of insulating clusters having either the same or smaller size relative to the wavelength distribution of THz pulse. Redistribution of insulating/metallic clusters can be further confirmed from real THz conductivity spectra of the film as described below.

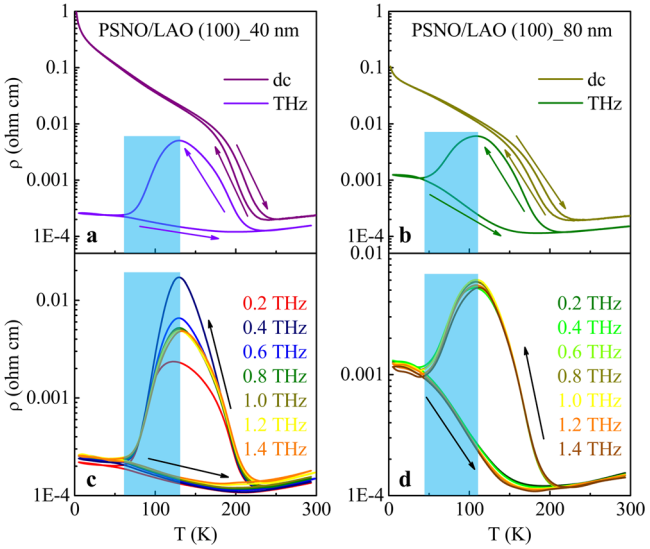

Fig. 3 Kinetically arrested phase transition. a, **b** Comparison of temperature-dependent resistivities obtained through dc transport and THz-TDS (at 1 THz). Arrows show heating and cooling sequences. The shaded region in THz conductivity shows kinetically arrested phase where the metallic phase reappears below T_{MI}. The kinetically arrested phase is detectable at all the THz frequencies shown by the shaded region in **c**, **d**.

A comparative representation of heating and cooling real conductivity spectra of PSNO/LAO (40 nm) film is shown in Fig. 4. It is clear that the conductivity spectra are significantly different for a given temperature in the hysteretic region collected while cooling and heating, while are same at all the temperatures beyond the hysteretic region. As seen in Fig. 4, before and after the hysteretic region, the real conductivity spectra for both heating and cooling data follow similar Drude-like behavior. In the hysteretic region, in contrast, though the conductivity in the

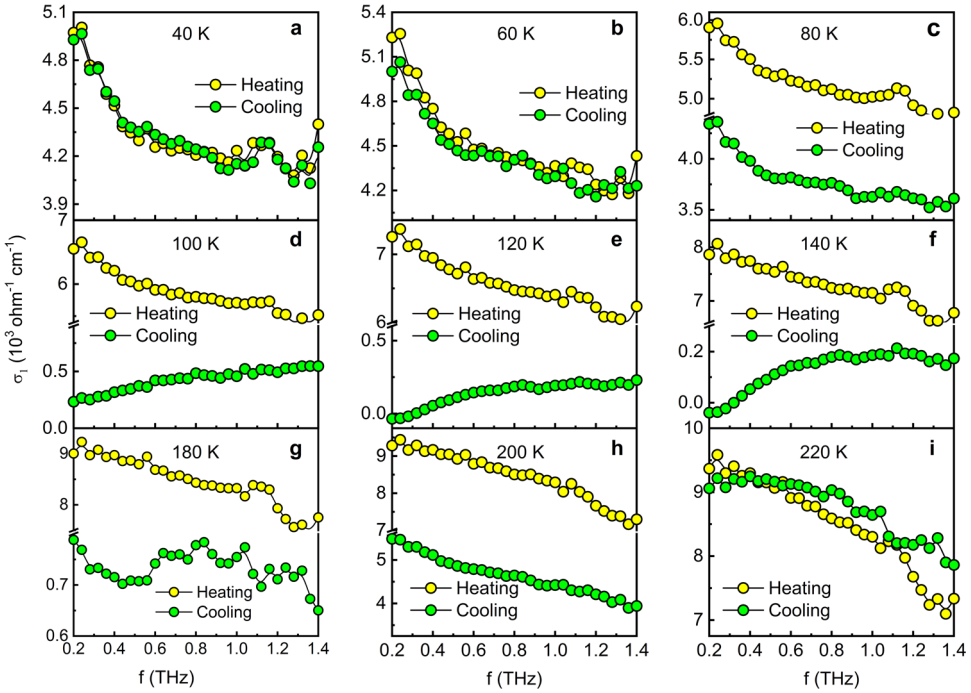

Fig. 4 Heating and cooling THz conductivity spectra for PSNO/LAO (100)_40 nm film. a–i Comparison of frequency-dependent real conductivity spectra obtained in heating and cooling sequences at various temperatures; within hysteretic region and beyond hysteretic region for PSNO/LAO (100)_40 nm film.

heating protocol continues to follow Drude-like behavior, in the cooling protocol, it exhibits a strong non-Drude-like behavior. While Drude behavior is expected in high-quality homogenous phases, the Drude-Smith type of conductivity manifests from enhanced scattering/backscattering of carriers due to phase inhomogeneity[20]. This implies that the phase transition in the heating protocol is quite smooth but in the cooling protocol, it is rather inhomogeneous and non-uniform. This supports the redistribution of insulating/metallic cluster sizes and occurrence of kinetically arrested phase transition during cooling[9,10,33–35]. Observation of kinetically arrested phase transition in THz transport also highlights the potential of THz spectroscopy in unravelling microscopic details during the phase transition.

We further increased the strength of disorder in PSNO film by growing it on a mosaic LAO substrate. A mosaic substrate consists of a large number of small perfect crystallites, of microscopical or sub-microscopical size, which are oriented almost, but not exactly parallel to each other[36]. This disorientation is usually only of 0.1–0.5^0. However, this slight disorientation creates extra grains, defects, and misfits in the substrate. As the thin film tends to acquire structural symmetry of the underlying substrate, the film formation on the mosaic substrate leads to the formation of extra grains, defects, and misfits in the film as well. This leads to the enhanced electronic inhomogeneity (or phase-coexistence) and scattering of itinerant charge carriers in the film. Consequently, the sharpness of the MIT in a mosaic film is reduced compared to a non-mosaic film. Thus, mosaic structure of the underlying substrate effectively works as a disorder. Figure 5 shows the comparison of DC and THz resistivities of the mosaic PSNO/LAO film. Here, once again we reach the same result: the DC transport shows MIT while the THz transport detects nearly metallic phase only (or very weak MIT compared to that in DC transport) in the entire temperature range. This affirms the generic nature of the response of the electronic phase-coexistence state to THz-TDS. Introduction of all types of disorder in thin-film motif yields the same result; i.e., strengthening of the metallic response in the THz transport. Above a critical

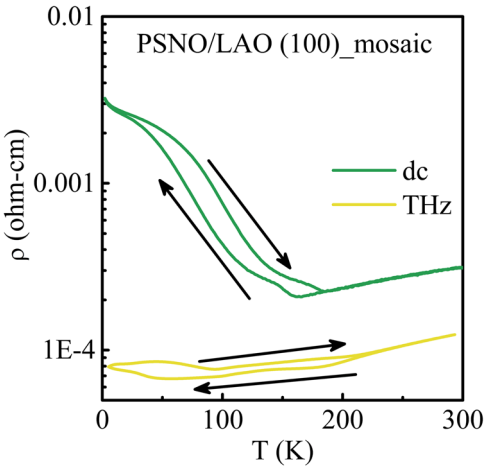

Fig. 5 Phase-coexistence in mosaic disordered film. Comparative representation of resistivities for PSNO/LAO (100) mosaic film, obtained through dc transport and THz-TDS (at 1 THz). Arrows show the path followed by data-points in heating and cooling sequences.

strength of disorder, the THz transport detects only the metallic state of the film. It may be noted that the electronic phase-separation is a prevalent feature of the first-order MIT, as is exhibited by many complex oxides such as manganites, nickelates, and vanadates[1]. Depending on the material system, the sources to induce electronic phase-separation and their underlying mechanisms might be different. Oxygen vacancies, crystal defects, polycrystalline disorder, mosaic disorder in thin films, etc., are some of such sources known in complex oxides. Validating our proposed methodology to detect electronic phase-separation in other complex oxides may serve as a confirmation that the present approach is independent of material systems, sources of disorder, and mechanisms inducing the electronic phase-

separation. With this confirmation, our methodology opens a scope for probing the electronic phase-separation in a large variety of material systems.

Conclusions

In summary, we demonstrated a comparative investigation of THz-TDS transport combined with DC transport to probe the complex electronic phase-coexistence. Upon modulating the insulating/metallic cluster sizes in the phase-coexistence state via introducing a controlled amount of disorder, DC transport continues probing the insulating state while THz-TDS probes weaker insulating state below the T_{MI}. Above a critical strength of disorder, only the metallic state is probed in the THz transport. The response of THz-TDS to electronic phase-coexistence is based on two factors, summed up as follows; (i) this technique shows extraordinary sensitivity in the detection of the spatial distribution of electronic phase-coexistence state when the insulating/metallic cluster sizes are comparable to or greater than the probing wavelengths of THz radiation, thus, bringing a large variety of materials under the characterization ambit of this technique, and (ii) average response to those clusters of sizes much smaller than the THz wavelength, thus, implying the capability of this technique to overlook such clusters. We hope our methodology will be fruitful in characterizing electronic phase-coexistence in a variety of systems and can shed more light in determining intricate mechanisms related to the phase transitions in complex materials.

Methods

Thin film growths. All the thin films were grown using pulsed laser deposition (PLD) technique. Optimized parameters were used in respective film growths to obtain films of the required disorder. Deposition parameters for different films can be found elsewhere[15,19,36,37]. All the substrates used for film growth were of 0.5 mm thick. The approximate thicknesses of the films are given in Table 1.

DC transport measurements. DC resistivity of all the films was measured using a physical property measurement system (PPMS) in the range of 2–300 K temperature. Measurements were performed in four-probe configuration to minimize the contact resistance.

THz time-domain spectroscopy (THz-TDS). THz-TDS measurements on the films were carried out in transmission mode using a photoconductive antenna-based spectrometer in the spectral energy range of ~0.8–6 meV. A schematic of our spectrometer and its measurement configuration is given in Supplementary Fig. 1. More details about the spectrometer, its working principle, and measurement procedure can be found in ref. [38]. The frequency-dependent THz optical properties were determined in the temperature range of 5–300 K. The THz data were collected at different fixed temperatures by passing the THz waveform first through vacuum, then through the substrate and finally through the film deposited on the very same substrate (see Supplementary Fig. 2a). To avoid any phase error, we processed the substrate in the same deposition condition which was to be used for the film growth before taking the measurements for the substrate. After then, film was grown on the same substrate, and the THz data were collected for the film. The spatial dimension of all the films for THz measurement was 10 mm × 10 mm.

Analysis of THz time-domain data. The THz waveform is typically collected as a function of a time-delay between the THz pulse and laser pulse reaching to THz detector. Typical THz temporal waveforms transmitted through vacuum (CRYO), substrate, and film are shown in Supplementary Fig. 2b. A brief procedure to extract THz conductivity from these temporal THz waveforms is as follows:

1. The time-domain waveform is converted into a frequency domain by fast Fourier transform (FFT) to obtain the amplitude and phase of the THz pulse as a function of THz frequency (Supplementary Fig. 2c).
2. Considering amplitude and phase of the THz pulse transmitted through vacuum as a reference, complex transmission coefficient of substrate with respect to vacuum is determined.
3. In the next step, complex transmission coefficient of the film with respect to vacuum is determined once it is determined for the substrate.
4. From the transmission coefficient, complex refractive indices of the film are determined.
5. Complex THz conductivity and dielectric constant of the film are determined from its complex refractive indices using the following relations:

$$\varepsilon_1 = n^2 - k^2, \varepsilon_2 = 2nk$$

$$\sigma_1 = \omega\varepsilon_0\varepsilon_2, \sigma_2 = \omega\varepsilon_0(\varepsilon_\infty - \varepsilon_1)$$

Here σ_1 and σ_2 are real and imaginary THz conductivities; ε_1 and ε_2 are real and imaginary dielectric constants, respectively; n and k are real and imaginary refractive indices; ε_0, ε_∞, and ω are vacuum permittivity, permittivity at very high frequency and THz angular frequency, respectively. For more detailed procedure, see ref. [39].

Structural analysis. We performed XRD θ–2θ scans and reciprocal space mappings (RSMs) of all the films to insure the quality and correct phase formation of the films. These measurements were performed on a PANalytical x-ray diffractometer at room temperature. Supplementary Fig. 3 shows (200) XRD θ–2θ intensity peaks of these films. All the film peaks are quite intense, indicating a good growth rate of the film in the optimized conditions used in respective film growths. The films grown on NGO (100) and LSAT (100) substrates are tensile strained while the films grown on LAO (100) substrate are compressively strained. Supplementary Fig. 4 shows RSMs of these films. It is clear that the film growth is coherent, epitaxial and all the films are in a nearly fully strained state as x-coordinates for film and substrate, in each case, are nearly the same (shown by the red dotted vertical line). The multiple peaks of substrate and film for the mosaic film are due to the mosaic crystal structure of the substrate.

Data availability

Data related to this study are available from the corresponding author upon reasonable request.

Received: 7 July 2021; Accepted: 29 June 2022;
Published online: 27 July 2022

References

1. Dagotto, E. Complexity in strongly correlated electronic systems. *Science* **309**, 257–262 (2005).
2. Shenoy, V. B., Sarma, D. D. & Rao, C. N. R. Electronic phase separation in correlated oxides: the phenomenon, its present status and future prospects. *ChemPhysChem* **7**, 2053–2059 (2006).
3. Kumar, K. S. et al. Terahertz electrodynamics in transition metal oxides. *Adv. Optical Mater.* **8**, 1900958 (2020).
4. Qazilbash, M. M. et al. Mott transition in VO_2 revealed by infrared spectroscopy and nano-imaging. *Science* **318**, 1750–1753 (2007).
5. Post, K. W. et al. Coexisting first- and second-order electronic phase transitions in a correlated oxide. *Nat. Phys.* **14**, 1056–1061 (2018).
6. Fath, M. et al. Spatially inhomogeneous metal-insulator transition in doped manganites. *Science* **285**, 1540–1542 (1999).
7. Gomes, K. K. et al. Visualizing pair formation on the atomic scale in the high-T_C superconductor $Bi_2Sr_2CaCu_2O_{8+\delta}$. *Nature* **447**, 569–57 (2007).
8. Roy, S. B., Chaddah, P., Pecharsky, V. K. & Gschneidner, K. A. Jr Overview No. 145 metamagnetic transitions, phase coexistence and metastability in functional magnetic materials. *Acta Materialia* **56**, 5895–5906 (2008).
9. Miao, X. F. et al. Kinetic-arrest-induced phase coexistence and metastability in (Mn,Fe)2(P,Si). *Phys. Rev. B* **94**, 094426 (2016).
10. Keavney, D. J. et al. Phase coexistence and kinetic arrest in the magnetostructural transition of the ordered alloy FeRh. *Sci. Rep.* **8**, 1778 (2018).
11. McLeod, A. S. et al. Nanotextured phase coexistence in the correlated insulator V_2O_3. *Nat. Phys.* **13**, 80–87 (2016).
12. Liu, S. et al. Random field driven spatial complexity at the Mott transition in VO_2. *Phys. Rev. Lett.* **116**, 036401 (2016).
13. Mattoni, G. et al. Striped nanoscale phase separation at the metal–insulator transition of heteroepitaxial nickelates. *Nat. Commun.* **7**, 13141 (2016).
14. Nikulina, I. V., Novojilova, M. A., Kaulb, A. R., Mudretsovab, S. N. & Kondrashovb, S. V. Oxygen nonstoichiometry of $NdNiO_{3-\delta}$ and $SmNiO_{3-\delta}$. *Mater. Res. Bull.* **39**, 775 (2004).
15. Das, S., Phanindra, V. E., Philip, S. S. & Rana, D. S. Unveiling the control of quenched disorder in rare earth nickelates. *Phys. Rev. B* **96**, 144411 (2017).
16. Pesquera, D. et al. Surface symmetry-breaking and strain effects on orbital occupancy in transition metal perovskite epitaxial films. *Nat. Commun.* **3**, 1189 (2012).

17. Aschauer, U., Pfenninger, R., Selbach, S. M., Grande, T. & Spaldin, N. A. Strain-controlled oxygen vacancy formation and ordering in $CaMnO_3$. *Phys. Rev. B* **88**, 054111 (2013).
18. Peng, J. J. et al. Manipulating the metal-to-insulator transition of $NdNiO_3$ films by orbital polarization. *Phys. Rev. B* **93**, 235102 (2016).
19. Phanindra, V. E. et al. Tuning the terahertz low-energy charge dynamics by simultaneous effect of epitaxial and anisotropic strain in $PrNiO_3$ thin films. *Phys. Rev. B* **95**, 085114 (2017).
20. Smith, N. Classical generalization of the Drude formula for the optical conductivity. *Phys. Rev. B* **64**, 155106 (2001).
21. Das, S. et al. Cation disorder and epitaxial strain modulated drude–smith type terahertz conductivity and hall-carrier switching in Ca_{1-x} Ce x RuO_3 thin films. *J. Phys. Condens. Matter* **29**, 025805 (2017).
22. Lee, S., Chen, R. & Balents, L. Landau theory of charge and spin ordering in the nickelates. *Phys. Rev. Lett.* **106**, 016405 (2011).
23. Rana, R., Pandey, P., Phanindra, V. E., Prabhu, S. S. & Rana, D. S. Terahertz spectroscopic evidence of low-energy excitations in $NdNiO_3$. *Phys. Rev. B* **97**, 045123 (2018).
24. Das, S., Prajapati, G. L., Anagha, P. & Rana, D. S. Terahertz charge dynamics unveil fundamental transport anisotropy in charge-ordered $Pr_{0.5}Eu_{0.5}NiO_3$ nickelate thin films. *Phys. Rev. B* **98**, 115110 (2018).
25. Das, S., Prajapati, G. L., Rana, R. & Rana, D. S. Probing low energy dynamics in charge-ordered $NdNiO_3$ by terahertz time domain spectroscopy. *Vacuum* **151**, 73–75 (2018).
26. Das, S., Prajapati, G. L. & Rana, D. S. Pinned and bound modes of charge density wave type collective excitation in $SmNiO_3$ as revealed by terahertz spectroscopy. *Phys. Rev. B* **102**, 214403 (2020).
27. Medarde, M. L. Structural, magnetic and electronic properties of $RNiO_3$ perovskites (R = rare earth). *J. Phys. Condens. Matter* **9**, 1679–1707 (1997).
28. Zhang, J. et al. Cooperative photoinduced metastable phase control in strained manganite films. *Nat. Mater.* **15**, 956 (2016).
29. Lai, K. et al. Mesoscopic percolating resistance network in a strained manganite thin film. *Science* **329**, 190 (2010).
30. Chaddah, P., Kumar, K. & Banerjee, A. Devitrification and recrystallization of magnetic glass $La_{0.5}Ca_{0.5}MnO_3$. *Phys. Rev. B* **77**, 100402(R) (2008).
31. Banerjee, A., Kumar, K. & Chaddah, P. Enhancement of equilibrium fraction in $La_{0.5}Ca_{0.5}MnO_3$ by recrystallization. *J. Phys. Condens. Matter.* **20**, 255245 (2008).
32. Ji, M., Davis, C. & Strangwood, M. Effect of grain size distribution on recrystallisation kinetics in an Fe-30Ni model alloy. *Metals* **9**, 369 (2019).
33. Chattopadhyay, M. K., Roy, S. B. & Chaddah, P. Kinetic arrest of the first-order ferromagnetic-to-antiferromagnetic transition in $Ce(Fe_{0.96}Ru_{0.04})_2$: formation of a magnetic glass. *Phys. Rev. B* **72**, 180401(R) (2005).
34. Rawat, R., Mukherjee, K., Kumar, K., Banerjee, A. & Chaddah, P. Anomalous first-order transition in $Nd_{0.5}Sr_{0.5}MnO_3$: an interplay between kinetic arrest and thermodynamic transitions. *J. Phys. Condens. Matter.* **19**, 256211 (2007).
35. Bar, T. et al. Kinetic spinodal instabilities in the mott transition in V_2O_3: evidence from hysteresis scaling and dissipative phase ordering. *Phys. Rev. Lett.* **121**, 045701 (2018).
36. Prajapati, G. L., Das, S. & Rana, D. S. Digital- to analog-type terahertz modulation controlled by mosaicity of the substrate template in rare-earth nickelate thin films. *ACS Appl. Mater. Interfaces* **11**, 33109–33115 (2019).
37. Phanindra, V. E., Kumar, K. S. & Rana, D. S. Anisotropy in static and terahertz dynamic conductivities across in-plane axes of lanthanum nickel oxide thin films. *J. Phys. D* **51**, 435302 (2018).
38. Dexheimer, S. L. *Terahertz Spectroscopy: Principles and Applications* (CRC Press, Boca Raton, 2007).
39. Neu, J. & Schmuttenmaer, C. A. Tutorial: an introduction to terahertz time domain spectroscopy (THz-TDS). *J. Appl. Phys.* **124**, 231101 (2018).

Acknowledgements

The authors acknowledge Prof. Richard Averitt for fruitful discussions. D.S.R. thanks the Science and Engineering Research Board (SERB), Department of Science and Technology, New Delhi, for financial support under research Project No. CRG/2020/002338. Financial support from DST-FIST and CSIR (File No. 09/1020 (0090)/2016-EMR-I) are also thankfully acknowledged.

Author contributions

G.L.P., S.D., R.D., and V.E.P. jointly worked in the experiments. G.L.P. and S.D. wrote the paper. D.S.R. supervised the overall work and in writing the manuscript.

Competing interests

The authors declare no competing interest.

Additional information

Supplementary information The online version contains supplementary material available at https://doi.org/10.1038/s43246-022-00271-1.

Correspondence and requests for materials should be addressed to Dhanvir Singh Rana.

Peer review information *Communications Materials* thanks the anonymous reviewers for their contribution to the peer review of this work. Primary Handling Editor: Aldo Isidori.

Reprints and permission information is available at http://www.nature.com/reprints

Publisher's note Springer Nature remains neutral with regard to jurisdictional claims in published maps and institutional affiliations.